Article:
Liu, Q orcid.org/0000-0002-1132-9392, Wang, C, Qian, J et al. (1 more author) (2023) Investigation of the early stage corrosion characteristics of molten (nitrate) salt – oxide – metal interfaces, and the links to interfacial thermo-mechanical stress. Corrosion Science, 220. 111282. ISSN 0010-938X

https://doi.org/10.1016/j.corsci.2023.111282

Investigation of the Early Stage Corrosion Characteristics of Molten (Nitrate) Salt – Oxide – Metal Interfaces, and the links to Interfacial Thermo-Mechanical Stress

Qingyang Liu[a,b,*] , Chun Wang[a,b], Jiong Qian[b,c], and Frederick Pessu[a,b].

a. Institute of Functional Surface, School of Mechanical Engineering, University of Leeds, Leeds, LS2 9JT, United Kingdom.

b. Jiuli Corrosion and Integrity Centre Laboratory (University of Leeds), Leeds, LS2 9JT, United Kingdom.

c. Engineering Research Centre of High-Performance Nuclear Power Pipe Forming of Zhejiang Province, Huzhou 313028, China

[*] Corresponding author: Qingyang Liu (Q.liu3@leeds.ac.uk & liuqingyang567@outlook.com)

Keyword:

Molten salt; Thermal stress; Stainless Steels; Nano-indentation; Multi-corrosion layer; Spallation;

Highlight:

- **Early-stage synergy of temperature and gas on overall corrosion were established.**
- **Thermo-mechanical stress effects across metal/oxide/interfaces were characterised.**
- **Inner tensile stress linked to $NaFeO_2$ directly correlates with the tendency for spallation to occur.**
- **Tests in Ar was observed to increase corrosion rate compared to test in air.**
- **Compressive stress linked to inner oxides and metal correlates to improved resilience of interface.**

Abstract:

This paper investigates the early-stage corrosion behaviour of 4 alloys in solar-salt under air and argon at elevated temperatures for 7 days. The multi-layered interfacial corrosion oxides were observed to consist of an inner Cr-rich oxide and an outer Na/Fe-rich oxide. The inner tensile stress between the interfacial oxide layers were observed to correlate to the spallation of the porous outer Na/Fe-rich oxide layer. The combination of chemical aggression of molten salt, high temperature and argon atmospheres, acts in synergy to increase the kinetics of

formation of Na/Fe–rich outer oxide layer, and it's tendency to degrade by spallation due to an inner tensile stress.

1. Introduction

During the last few decades, efforts have been made to mitigate the progress of climate change through reduction of CO_2 emissions, and transitioning from the use of conventional coal-fired and/or fossil fuel power plants to renewable energy power [1]. The exploitation of solar energy has gained much more interests than other kinds of renewable energy sources due to the availability, accessibility and inexhaustibility of solar thermal irradiation. This has helped to significantly promote the development of the solar thermal energy conversion systems. Concentrated solar power (CSP) plants, accompanied with thermal energy storage (TES) systems, are the most promising and most widely used energy conversion plants, with the potential to meet a variety of energy intensive industrial needs. It works by transferring the abundant but intermittent solar thermal energy to continuous, dispatch-able and stable solar thermal electricity [2, 3]. Due to its high potential efficiency, low operation cost and low environmental impact [4], solar power collector technology is the foundation of commercial CSP systems where molten salts are widely used as heat transfer fluids (HTFs) and thermal storage material, and usually in direct interaction with metallic materials used as heat collectors, heat exchangers/transfer pipes, and hot storage tanks [3, 5, 6]. Nitrate salts (60 wt % $NaNO_3$ and 40 wt % KNO_3 also known as 'Solar salt'), is widely employed in CSP plants due to its good thermal-physical properties; such as high heat capacity, high thermal conductivity, wide working temperature range, high viscosity and low cost [6-8].

However, the low thermal stability of nitrate salt mixtures restricts the maximum operation temperature in CSPs, and hence restricts its efficiency. Rapid decomposition of nitrate ions into nitrite ions and further into soluble oxides and gaseous nitrous oxides occurs by Equation 1 and Equation 2 [9, 10] at temperature exceeding 600˚C. This has already been confirmed using XRD analysis of salts before and after experiments in a previous publication [11].

$$NO_3^- \rightleftharpoons NO_2^- + \frac{1}{2}O_2(g) \qquad \text{Equation 1}$$

$$2NO_2^- \rightleftharpoons NO_2(g) + NO(g) + O^{2-} \qquad \text{Equation 2}$$

The chemical compositions of the salts changed due to the reactions above and thus altered the thermo-properties of molten salt. Worse still, this increases the oxidising and corrosive

tendencies of the molten salt species to increase rate of degradation of structural metallic materials used in CSP systems [12-15], particularly at temperatures above its thermal stability temperatures. The effect of temperature on the corrosive tendencies of molten salts has also recently gained increased interest with the push towards the super-critical CO_2 (Brayton) power cycles that would require outlet temperatures from solar receiver towers in excess of 700 ˚C. This is aimed at increasing efficiency of next generation CSP systems and reducing the levelized cost of electricity (LCOE) [16]. However, this can only be delivered with more aggressive salt types such as chloride and carbonate salts [17].

Several other research have been summarised by Walczak.et.al [8] on the corrosion performance of carbon/low-alloys steel, stainless steels and Ni-based alloys with different salts at different temperatures. It was shown that the corrosion rate and the thickness of corrosion oxide layer increase with increase of temperature [8]. Alan [18] investigated the corrosion of alloys at 400, 500 and 680˚C in Solar salt and found significant alloy surface degradation occurring at a corrosion rate above 450 µm/year at 680˚C, almost 10 times higher than that at 500˚C. Pieces of research shown in Figure 1, was explored to mitigate the corrosion process by controlling the gas atmosphere [19, 20]. Vignarooban [20] found that corrosion rate of C-276 after 42 day-immersion test in open container at 500˚C was 10 times higher than in sealed container at 800˚C. On the other hand, S.Bell et.al [21] reported that the corrosion was even more severe for C-276 tested with chloride/sulphate eutectic salt in argon than that in air. Therefore, they concluded that the gas atmosphere plays a significant role in directing the corrosion characteristics of a molten-salt - alloy interface. In terms of designing tests to simulate conditions as closely as in real CSP systems, longer duration tests in excess of 1000 h are usually favoured [8, 22, 23]. However, a 7-day duration has been chosen for this study to represent the early stage of the evolution of the molten salt – metal corrosion interface. The purpose and focus of this study on investigating the early stages of corrosion and interfacial oxide formation during molten salt – metal interactions is hinged on the fact that at this early stages, the corrosion process is usually initial impurity-driven, and always results in higher corrosion rate [16]. In a previous study [11], it was also confirmed that the stainless steels and Ni-based alloys corrosion exhibited severe corrosion with higher corrosion rate and thicker corrosion scale at 600˚C in argon. That's the reason why 7 day was chosen for this study.

Some recent literatures on oxidation of alloys [24, 25] suggested that mechanical properties of the surface oxide layers were also critical in determining its capacity to protect the substrate

against further oxidation. This was on the premise that the main factor influencing the oxidation resistance of the alloys is the mechanical integrity of the surface oxide layer [26]. This could be linked to internally built - up of stresses [27] that arises naturally during the oxidation process; due to the difference in specific volume of oxide and substrate metal, and on thermal stresses that emerges during cooling; due to different thermal expansion/contraction coefficients between surface oxide layers and substrate [28].

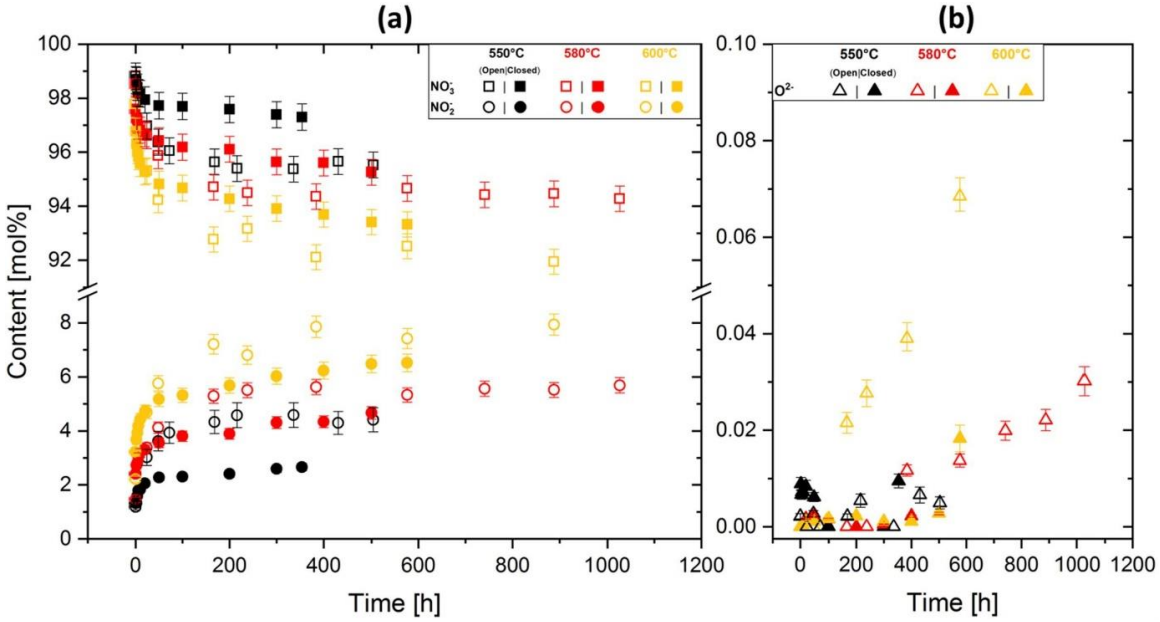

Figure 1 Nitrate and nitrite content in Solar Salt stored in open atmosphere (open symbols) and closed atmosphere (closed symbols) at 550°C, 580°C and 600°C. Adapted from Ref [19]

Therefore, in order to fully understand the corrosion behaviour of molten salt – metal interface systems, the adherence, protectiveness and nano-mechanical properties of the interfacial oxide layers need to be carefully investigated and characterised. This can be correlated to the tendency for material degradation by spallation, manifested as loss of corrosion resilience at molten salt – metal interfaces. This study experimentally investigated the corrosion behaviours of two stainless steel and two Ni-based alloys at 565˚C and 600˚C under air and argon atmospheres using a combination of gravimetric (weight loss) analysis, advanced surface and subsurface characterisation techniques; including nano-mechanical characterisation. This study investigates the formation and protectiveness of corrosion oxide layers in the context of the synergistic effect of temperature and gas atmospheres on the overall corrosion process based on a total test duration of 7 days (168 h). A key part of this study is the investigation of the interfacial stress profile across the molten salt – oxide – metal interface. The results from this aspect of the study will help in correlating the thermal stress profile across the interface with the rate and tendency of oxides spallation during molten salt induced corrosion processes.

Detailed microstructural characterizations and other methods deployed in this study are provided in the subsequent sessions in this paper.

2. Experimental Procedure

2.1 Material and methods

Stainless steel (AISI 321 and 347) and Ni-based alloys (Alloy 625 and Alloy 825) are used in the following experiments and the compositions are provided in Table 1. The samples were cut from corresponding seamless pipes supplied by Zhejiang JIULI Hi-tech Metals Co., Ltd with a dimension of 25 mm x 13 mm and 3 mm thick. The samples were prepared by grinding with silicon carbide paper up to P1200 (600 grit, Ra: 0.11 µm) and polishing with 9 µm, 6 µm, 1 µm and 0.25 µm diamond suspension to a mirror-like surface, rinsed with acetone and deionized (DI) water, then dried using hot-air. The prepared samples were weighed on an analytical balance with an accuracy of 0.01mg and then kept in a desiccator for a short time before the test to prevent any pre-experiment oxidation.

Solar salt (60 wt. % $NaNO_3$ and 40 wt. % KNO_3) from Alfa Aesar was used for this study with analytical reagent purity (the detailed components and impurities of solar salt is provided in the supplementary file). The salts were weighed to achieve the required ratio, mixed to achieve homogeneity, and put into four crucibles to dry at 180°C for 24 h in an oven (gas-controlled furnace for test under argon atmosphere) [29] before the commencement of experiments. According to British Standard ISO 17245:2015, the total amount of solar salt for each crucible is 413 g to meet the required volume / surface area ratio (20 ml per 1 cm^2 of samples' area).

Table 1: Alloy composition of AISI 321 and 347, IN 625 and In 825 (wt. %).

Alloy	C	Mn	Si	P	Cu	Cr	Ni	**Ti**	**Nb**	Mo	Fe
AISI 321	0.018	1.44	0.519	0.035	-	17.33	9.24	0.225	-	-	Bal.
AISI 347	0.049	0.95	0.402	0.026	0.11	17.35	9.65	-	0.656	-	Bal.
IN 625	0.018	0.04	0.142	0.001	0.03	21.69	62.36	0.211	3.31	8.65	3.06
In 825	0.008	0.67	0.258	0.0119	1.75	22.6	40.18	0.943	0.025	2.88	30.32

Samples of each alloy retrieved from desiccator were carefully placed in the salt with the help of tweezers in four Al_2O_3 crucibles (OD 140mm, 70mm height) to ensure consistent contact surface areas between the samples and molten salt. The crucibles (with salt and samples) were kept inside the oven for extra 12 hours to allow the required Ar gas flowing through for fully established Ar atmosphere. Then the oven was gradually heated up to test temperature (565 and 600°C for this study) and kept for 7 days (168 h) within the chamber under either air or Ar

atmosphere. 6 parallel samples of each alloy are used in this study and 3 samples are washed and weighed for corrosion rate calculation and others go through microstructural analysis.

2.2 Corrosion Product Analysis

The methodology used in calculating the mass loss and corrosion rate of the samples after the test has already been defined in previous study [11] and provided in supplementary files. The top-view and cross-sectional morphology of the interfacial corrosion oxides were observed using Scanning Electron Microscope (SEM) with Energy Dispersive Spectroscopy (EDS). The chemistries of interfacial corrosion oxides were assessed using a combination of X-Ray Diffraction (XRD) spectrum and Raman spectroscopy. The XRD penetration depth are around 19.9 μm for stainless steel and 17.6 μm for Ni-based alloys at 90° incident angle (from software 'Highscore'). For Raman spectroscopy, the Renishaw InVia spectrometer (UK) was used in this study. 488 nm wavelength laser operated at a laser power of 0.1 and 0.5 mW with 50x short distance objectives.

The nano-mechanical properties of interfacial corrosion oxide layers and base material were analysed after nano-indentation test. The tests were performed using a Micro-materials Vantage platform equipped with a Berkovich tip. Indentations were made at more than 15 preselected points at 20mN maximum load. Loading and unloading were at fixed time of 15 seconds, with a dwell time of 5 sec to allow elastic relaxation of the materials before unloading. Hardness (H) and reduced modulus (E_r) were determined using the Oliver and Pharr method [30]. The Young's (elastic) modulus of the material being measured can then be determined using Equation 3,

$$\frac{1}{E_r} = \frac{(1-v^2)}{E} + \frac{(1-v_i^2)}{E_i} \qquad \text{Equation 3}$$

Where E_r is the reduced modulus, v_i and E_i are the Poisson's ratio and modulus of the indenter tip respectively, and v and E are the Poisson's ratio and elastic modulus of the sample. The diamond Berkovich indenter tip was assumed to have E_i=1141 GPa and v_i= 0.07.

2.3 Methodology of residual stress calculation

As previously mentioned in this paper, there are potential internal stresses across the interfacial oxide layers linked to their growth mechanism, and thermal stress related to the conditions at

the corroding interface. The internal stress induced by oxide growth is due to the fact that the specific volume of the oxide is rarely the same as that of the substrate metal [27], and can be mathematically related to the Pilling-Bedworth ratio (PBR) in Equation 4:

$$PBR = \frac{V_{ox}}{V_m} \quad \text{Equation 4}$$

Where V_{ox} and V_m represent the Volume of oxide and metal. Generally, the oxide is expected to be under compressive stress if PBR > 1 (the case for most metals), while the tensile stress develops in oxide scale with PBR < 1 [24, 28]. Generally metal – oxide interfaces with tensile stresses in the oxide cannot maintain protective films, e.g., K, Mg, Na. The PBR of NiO, Cr_2O_3 and Fe_2O_3 are 1.65, 2.07 and 2.14 respectively [28], indicating the protective nature of these oxide layer.

In addition, the thermal stress is generated during changes and fluctuations in the thermal profiles across the corroding interfaces due to the difference in the thermal expansion coefficient of the metal and oxide [28].

Note: The authors acknowledge the difficulty in isolating the stress effects due to oxide formation at high temperature and the stress contribution from the cooling of the test specimen at the end of the experiment. It is therefore assumed that both high temperature oxide formation process and cooling of test specimen contribute to the total thermal stress effects at the molten salt – oxide – metal interface, and hence, the overall spallation behaviours of the interfacial oxide layers. This has also been considered collectively in the terms of Equation 5.

The thermal stress caused by the thermal expansion misfit can be expressed by the Equation 5 [28] (the derivation part is provided in supplementary files):

$$\sigma_{Ox} = \frac{-(\alpha_{Ox} - \alpha_M)\Delta T}{\frac{2t_{Ox}(1-\gamma_M)}{t_M E_M} + \frac{(1-\gamma_{Ox})}{E_{Ox}}} \quad \text{Equation 5}$$

Where σ is the stress of the oxide formed for different thermal profiles.

α_M and α_{Ox} are the linear thermal-expansion coefficients for the metal and oxide (assumed constant), respectively. $\Delta T = T_L - T_H$ is the difference between the oxide formation temperature (T_H) and cooling temperature at the end of experiment (T_L), and thus the negative in sign in Equation 5; t_M and t_{Ox} are the thickness of metal and a single-oxide scale respectively. γ_M and γ_{Ox} is the Passion ratio of the metal and oxide, respectively. E_M and E_{Ox} are the elastic modulus of the metal and oxide, respectively.

Referring to Equation 5, the ΔT is assumed negative and α_{Ox} is typically $< \alpha_M$, and the resultant stress (negative sign) in the oxide is typically compressive.

3. Results

3.1 The comparisons of corrosion rate measurements

Figure 2 shows the measured weight loss and corrosion rate of stainless steel and Ni-based alloys after 7 – day immersion test at 565 and 600˚C under air and argon atmospheres. The results showed an expected trend of higher corrosion rate of stainless steels than Ni-based alloys in molten salt conditions, as well as an expected general increase in corrosion rate with increase in temperature from 565 to 600˚C in air. This along with the error bars from Figure 2 repeated experiments helps to demonstrate the reliability and repeatability of the experiments.

It is also important to note that the highest corrosion rate was recorded after immersion test at 600˚C under Ar atmosphere for all alloys; ~ twice as high as the corrosion rate of test under air atmosphere for AISI 321, 347 and In 825, and ~ 10 times higher for IN 625. For IN 625, the corrosion rate increases from 11.9 µm/y in the air to 128 µm/y under Ar atmosphere at 600˚C. Although IN 625 has been reported to have a superior corrosion resistance compared to stainless steels [18, 31] in air below 600˚C with corrosion rate of 12.7 µm/y, however, such superiority in corrosion resistance reduces at temperatures in excess of 680˚C in air with corrosion rate of 594 µm/y. For AISI 321, AISI 347 and In 825, the corrosion rate was observed to increase steadily with temperature and with change of gas atmosphere from air to Ar at 600˚C in Figure 2 after 7 days.

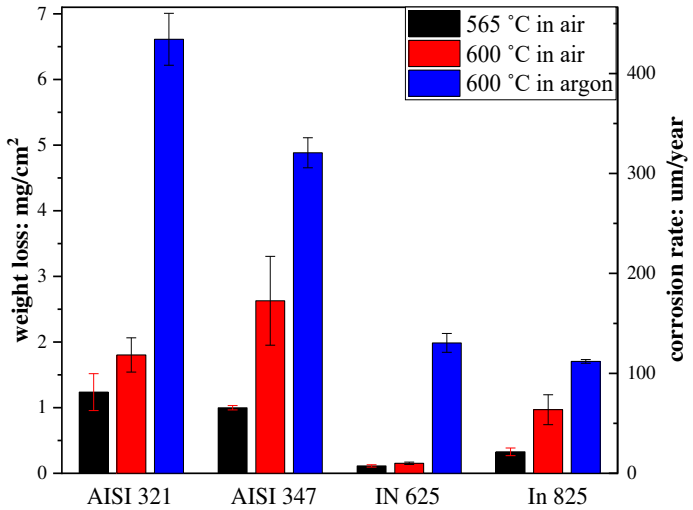

222 ***Figure 2 Mass loss (and corrosion rate) of AISI 321 AISI 347 IN 625 and In 825***
223 ***specimens at different temperature and atmosphere in solar salt for 7 days***

224 3.2 Corrosion Oxide Characterisation – XRD Analysis

225 According to the XRD analysis, the chemistry of corrosion oxides formed on the surfaces of
226 both stainless samples; AISI 321 and 347 in air are similar, with the only difference being in
227 terms of the intensity of the identified reflections. Based on the XRD results shown in Figure
228 3 (a1) (a2) (b1) (b2), it can be concluded that the interfacial corrosion oxide layers consist of
229 iron oxide (Fe_2O_3), iron chromium spinel ($FeCr_2O_4$), sodium ferrite ($NaFeO_2$), iron chromium
230 oxide and chromium oxide (Cr_2O_3). XRD patterns show more variability in oxide chemistry at
231 600˚C than at 565˚C, indicating the formation of a more complex combination of oxide spinel
232 at 600˚C. In contrast to the corrosion oxides formed under Ar atmosphere (Figure 3 (a3), (b3)),
233 the Cr-containing oxide was present only in form of $FeCr_2O_4$ without forming Cr_2O_3. This is
234 related to the oxide forming corrosion reaction most thermodynamically affected by the
235 availability of oxygen/oxide ions. The corrosion oxides formed on the surface of IN 625 in air
236 is mainly NiO, while Cr_2O_3 and $FeCr_2O_4$ was identified on the surface of IN 625 samples under
237 Ar. This finding correlates well with weight loss results in Figure 2, where IN 625 samples
238 under Ar atmospheres exhibited higher corrosion rate which is directly linked to increased
239 number of interfacial corrosion oxides formed on the surface. The main corrosion oxides
240 formed on In 825 are NiO, Fe_2O_3, $FeCr_2O_4$ and Cr_2O_3. $NaFeO_2$ was formed when test was
241 performed at 600˚C under air and Ar atmospheres, indicating the effect of both temperature
242 and gas atmospheres on the formation kinetics of $NaFeO_2$.

243 3.3 Corrosion Oxide Characterisation – SEM Surface Analysis

244 The oxide layers formed on the surface of samples are expected to provide some level of
245 protection to the base metal from continuous molten salt penetration. Therefore, interfacial
246 oxide formation process and mechanisms are critical to the overall corrosion mechanism at the
247 molten salt – metal interface. The SEM images of the top surface and possible oxide phases
248 from EDS analysis are shown in Figure 4 and provided in Table 2 respectively. Referring to
249 Figure 4 (a1) (b1) (c1) and (d1) for immersion test in air at 565˚C after 7 days, the corroded
250 surfaces of stainless steels appears to be smooth with only tiny and localized bulge in the
251 stainless steel samples, while the Ni-based alloy surface shows little difference from un-
252 corroded samples with visible evidence of polishing marks. This indicates that the corrosion is
253 mild in air at 565˚C after 7 days. Referring to Figure 4 (a2) (a3) (b2) and (b3) for the stainless-

steel samples tested at 600˚C in air and under Ar atmosphere, thicker but less compact corrosion oxide layers with evidence of layer spallation were observed on metal surface at 600˚C than that formed at 565˚C. This can be confirmed from EDS analysis shown in Table 2 (spectrum "S2" and "S3" for AISI 321, and "S6" and "S7" for AISI 347). The top-surface oxide layer on metal surface under Ar atmosphere was less compact with evidence of a more severe spallation than in air at 600 ˚C. The morphology and chemistry of corrosion oxides are also different (see Table 2; spectrum "S3" and "S4" for AISI 321, and "S6" and "S8" for AISI 347). Similar trend was also observed for In 825 and IN 625. Significant change in surface morphology of oxide layers was observed on the IN 625 with change of gas atmosphere from air to Ar at 600˚C, shown in Figure 4 (c2) and (c3). For In 825 the corrosion oxide layer formed on sample under Ar atmosphere at 600˚C showed dispersed particles of corrosion oxides, while needle-like corrosion oxides and crystalline oxide grains were randomly dispersed on the surface of In 825 after test in air. The top surface corrosion oxide layer was also observed to be more porous when sample is exposed to Ar atmosphere than in air as shown in Figure 4 (d2) and (d3).

3.4 Corrosion Oxide Characterisation; Cross -Sectional Surface Analysis

The cross-sectional analysis using the SEM was conducted to investigate the distribution of corrosion oxides across metal – oxide interface. This is presented in Figure 5.

Referring to Figure 5 (a1) (b1) (c1) and (d1), only a few corrosion oxides were identified from EDS cross sectional analysis on samples' surfaces after immersion test in air at 565˚C. This is consistent with XRD patterns shown in Figure 3, and indicating low corrosion rate under this condition. The thickness of oxide layers formed on stainless steels increased from ~ 3.5 to 10.5 µm with increase in temperature from 565 to 600˚C in air. There is also evidence of detachment and/or spallation of interfacial oxides in the form of an inner crack in Figure 5 (a2) (b2). When samples are exposed to Ar atmospheres at 600˚C, the corrosion oxide layer formed on AISI 321 is composed of two layers: an outer non-uniform layer of thickness of ~ 12 – 35 µm, and an inner layer of thickness of ~13 µm. This is shown in Figure 5 (a3). The outer layer was identified as Fe_2O_3 and $NaFeO_2$ (referring to Figure 5 (a3) and Table 2, "S4"), while the inner layer was a mixture oxide of (Fe, Cr): $FeCr_2O_4$ spinel. Similar double oxide layers were observed on AISI 347 with ~8 µm thick outer Fe_2O_3 layer and ~ 8 µm thick inner $FeCr_2O_4$ layer, as shown in Figure 5 (b3). For IN 625, no significant differences were observed between test at 565 and 600°C in air, while a 6 µm thick double layer was observed on surface of sample exposed to Ar atmosphere at 600°C. This double oxide layer consists of an outer mixed oxide

of Fe and Ni, and inner oxide of Cr. For In 825, a thin inner oxide layer was observed after immersion test in air at 600˚C, consisting of Fe_2O_3 layer and some crystalline copper oxide (the copper from In 825 substrate itself in Table 1) dispersed on the top layer, as shown in Figure 5 (d2). The thickness of corrosion oxide layer formed on the In 825 samples under Ar atmosphere ranges from 9 -13 μm, and also consist of an inner mixed oxides of Cr and Ni.

3.5 Corrosion Oxide Characterisation – Raman Analysis

Raman measurement was used to identify the corrosion oxides and support the results from XRD analysis. The Raman spectra and referred Raman shifts are shown in Figure 6 and Table 3. Figure 6 (a) and (b) indicates that the $NaFeO_2$ and Fe_2O_3 forms as the outmost oxide layers on stainless steels, while the inner layer consists of Cr_2O_3 and $FeCr_2O_4$ spinel. The corrosion oxides formed on the surface of IN 625 are Cr_2O_3 and a mixed oxide of Fe and Ni (identified as $NiFe_2O_4$ ($NiO\text{-}Fe_2O_3$)), shown in Figure 6 (c). The main corrosion oxides formed on the In 825 surface were identified as Fe_2O_3, Cr_2O_3 and $NiO\text{-}Fe_2O_3$ in Figure 6 (d). All of the Raman spectra correlate well with the results from XRD analysis.

3.6 Analysis of Stresses within Interfacial Corrosion Oxide Layers

Table 4 lists the coefficients of thermal expansion (CTE) of some common oxides and the studied alloys. However, due to the similarity in the chemistry of the corrosion oxide layers and the variation in their thickness at different temperatures and test atmospheres, the samples from test under Ar atmosphere at 600˚C were used for the nano-indentation test. This was because this condition provided samples with large enough thickness of the interfacial corrosion oxide layers for this analysis. Figure 7 (a) shows the load-displacement (P-h) curves obtained on the cross-sections of oxides formed on the alloys in this study. Based on the P-h curves, hardness H and elastic modulus E of the base metal, inner corrosion oxide layer and outer oxide layer were calculated using Oliver-Pharr method [32] and the results were plotted in Figure 7 (b).

The thermal stress values obtained using Equation 5 for the stress between inner layer and bulk material and between inner layer and outer layer were presented in Table 5. Referring to Table 5 for calculated thermal stress values:

σ_1 represents the stress between the inner oxide layer and bulk substrate for samples under Ar atmosphere at 600˚C.

$\boldsymbol{\sigma'_1}$ represents the stress between inner oxide layer and outer oxide layer for samples under Ar atmosphere at 600˚C.

σ_2 represents the thermal stress between inner oxide layer and bulk substrate for samples in air at 565˚C.

$\boldsymbol{\sigma'_2}$ represents the thermal stress between inner oxide layer and outer oxide layer for samples in air at 565˚C.

σ_3 represents the stress between the inner oxide layer and bulk substrate for samples in air at 600˚C.

$\boldsymbol{\sigma'_3}$ represents the thermal stress between inner oxide layer and outer oxide layer for samples in air at 600˚C.

Details of calculation is shown in the supplementary files.

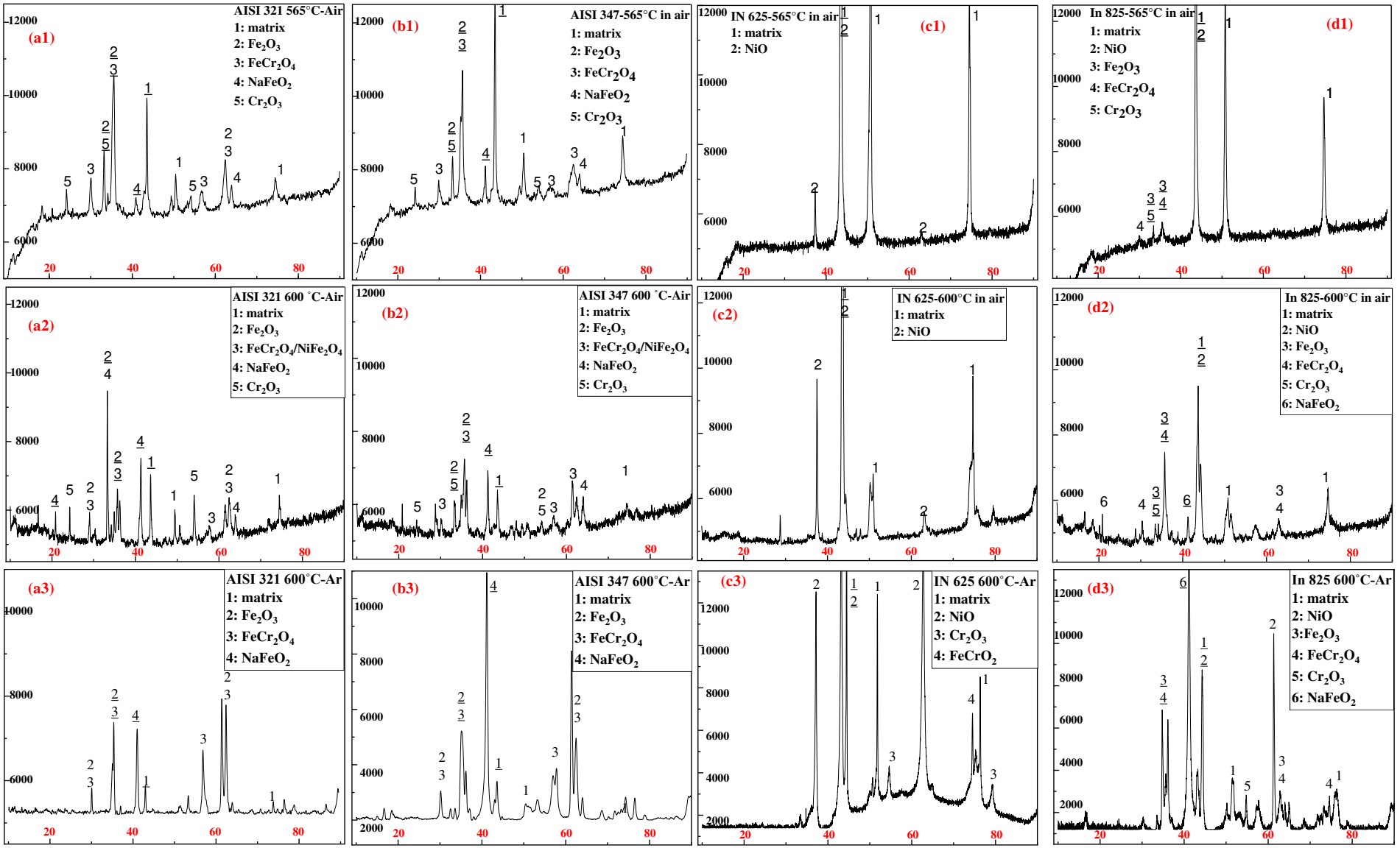

Figure 3 XRD patterns of studied alloys under different immersion conditions (phase number with underline meaning the 100% intensity reflections), (a) AISI 321, (b)AISI 347, (c) IN 625 and (d) In 825 after 7-day immersion test in Solar salt at (1) 565°C in air (2)600°C in air (3)600°C in argon, respectively (X-axis:2 theta in degree, y-axis intensity).

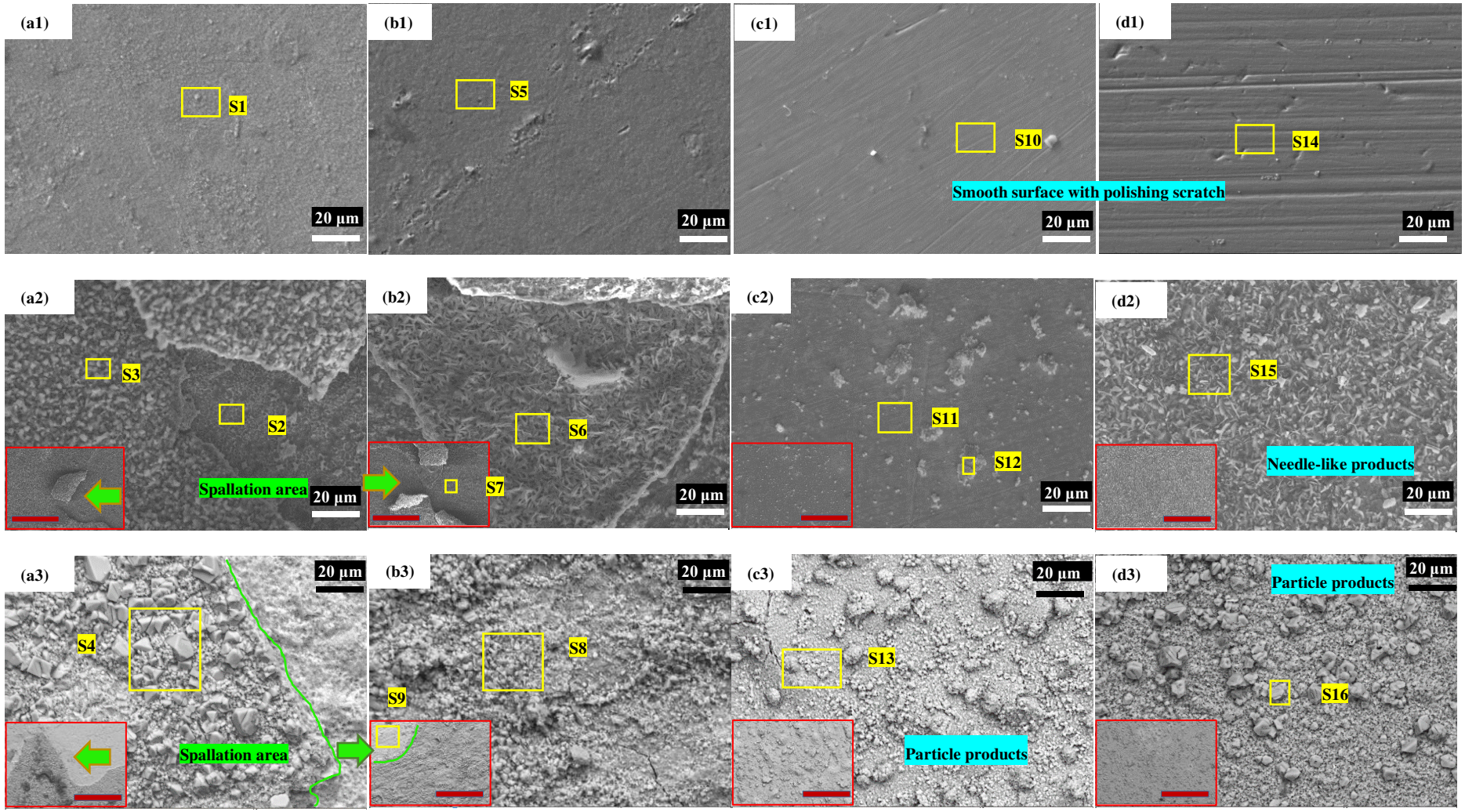

Figure 4: SEM top surface of the oxide scales formed on (a) AISI 321, (b)AISI 347, (c) IN 625 and (d) In 825 after 7-day immersion test in Solar salt at (1) 565˚C in air (2)600˚C in air (3)600˚C in argon, note: the red scale bar on the inlays figure indicates 200 µm.

336 ***Table 2 EDS data for regions and possible phase in Figure 4***

Element in wt%	Possible phase	Fe	O	Cr	Ni	Na
S1	$FeCr_2O_4$, Fe_2O_3	60.1	18.9	12.1	-	0.1
S2	$FeCr_2O_4$, Fe_2O_3	50.1	22.9	20.6	4.4	0.5
S3	$NaFeO_2$, Fe_2O_3	54.7	20.2	1.4	0.2	22.6
S4	$NaFeO_2$, Fe_2O_3	49.99	32.4	0.62	0.32	6.73
S5	$FeCr_2O_4$, Fe_2O_3	69.8	17.9	12.1	10.1	0.2
S6	$NaFeO_2$, Fe_2O_3	60.7	21.8	1.2	0.6	13.8
S7	$FeCr_2O_4$, Fe_2O_3	66.1	21.1	8.7	2.6	-
S8	$NaFeO_2$, Fe_2O_3	50.64	29.86	0.62	2.99	9.99
S9	$FeCr_2O_4$, Fe_2O_3	51.29	28.78	8.52	4.71	1.43
S10	NiO	2.6	7.1	16.2	54.0	-
S11	NiO	3.0	18.9	4.3	71.8	-
S12	NiO, $(Fe, Cr)_2O_3$	11.6	25.9	2.4	46.4	8.7
S13	NiO, $(Fe, Cr)_2O_3$	7.45	21.53	1.1	60.8	2.08
S14	NiO, $(Fe, Cr)_2O_3$	28.5	8.9	18.6	38.8	-
S15	NiO, Fe_2O_3,$NaFeO_2$	39.1	23.7	8.5	12.8	9.9
S16	NiO, Fe_2O_3,$NaFeO_2$	39.6	34.19	1.04	6.78	9.11

337

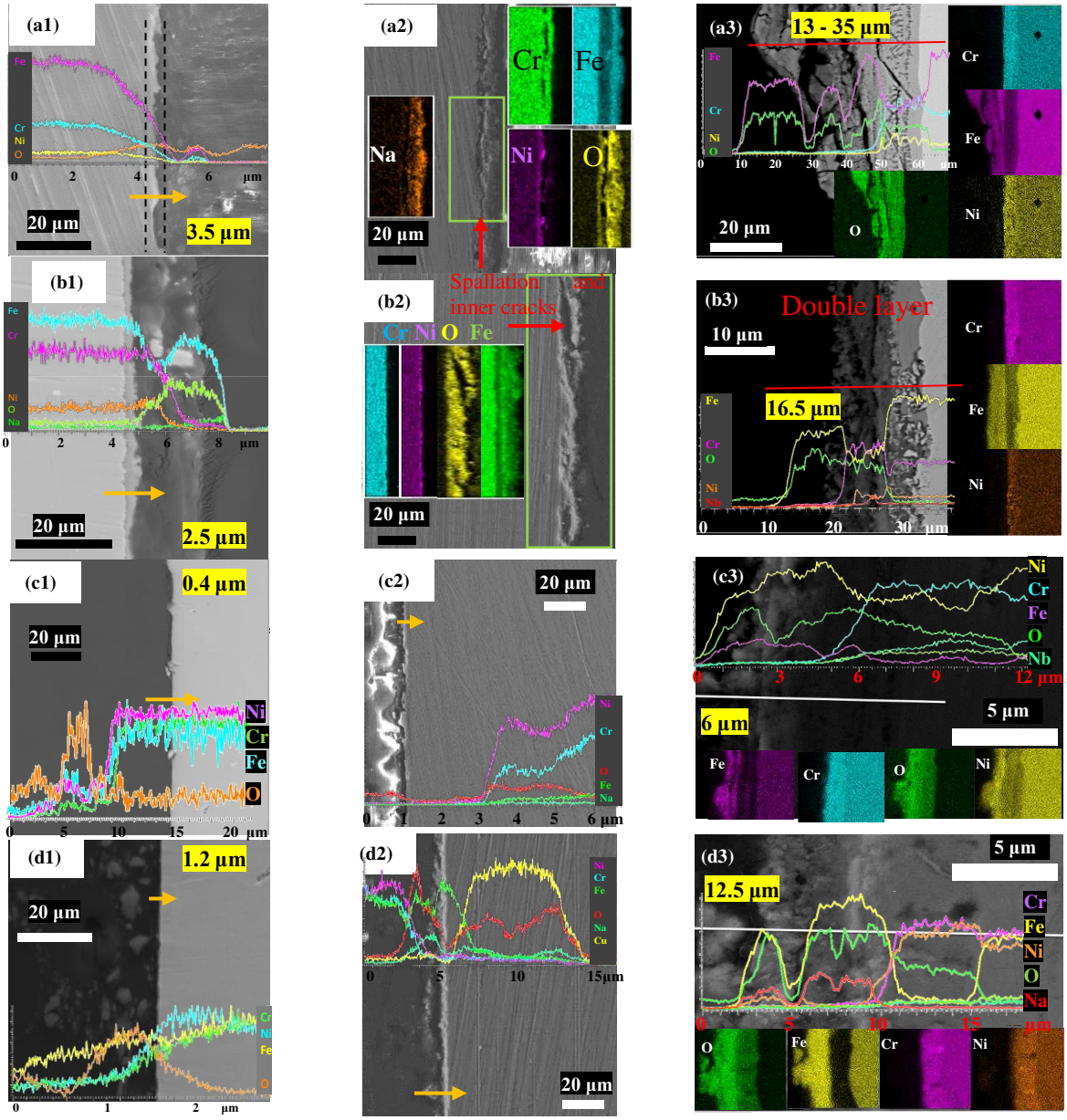

***Figure 5**: SEM-EDS profile of the oxide scales formed on (a) AISI 321, (b)AISI 347, (c) IN 625 and (d) In 825 after 7-day immersion test in Solar salt at (1) 565˚C in air (2)600˚C in air (3)600˚C in argon.*

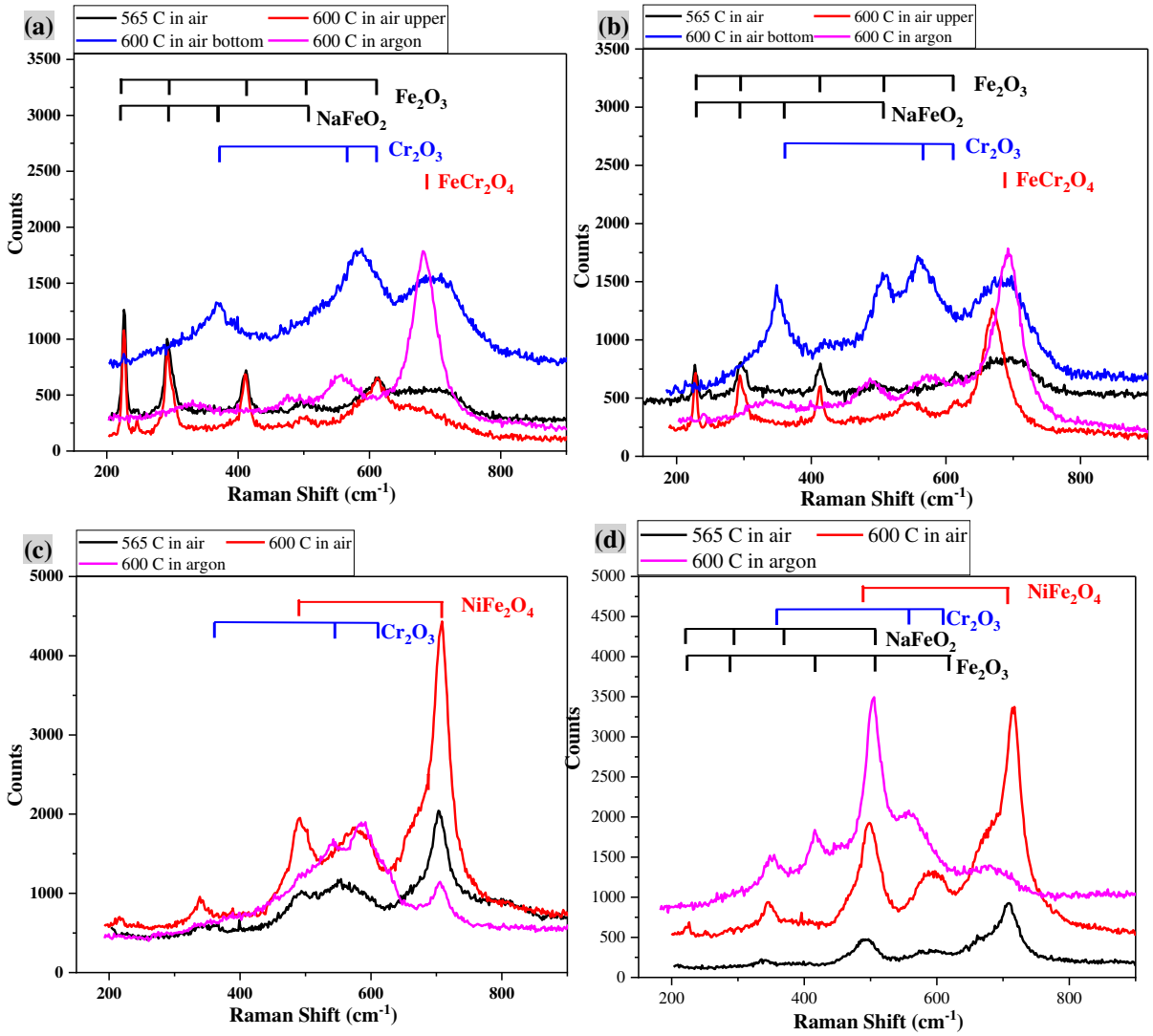

Figure 6 The detected Raman spectra for the development of the corrosion product scales on studied alloys (a):AISI 321, (b):AISI 347, (c) IN 625 and (d) In 825 at various conditions.

Table 3 Raman frequencies (cm^{-1}) of the oxides studied from literature [33-36]

Oxides	Raman shifts cm^{-1}
Fe_2O_3	225, 290, 411, 501, 610
$NaFeO_2$	220, 290, 350, 507
Cr_2O_3	353, 550, 616
$FeCr_2O_4$	686
$NiFe_2O_4$	487, 704

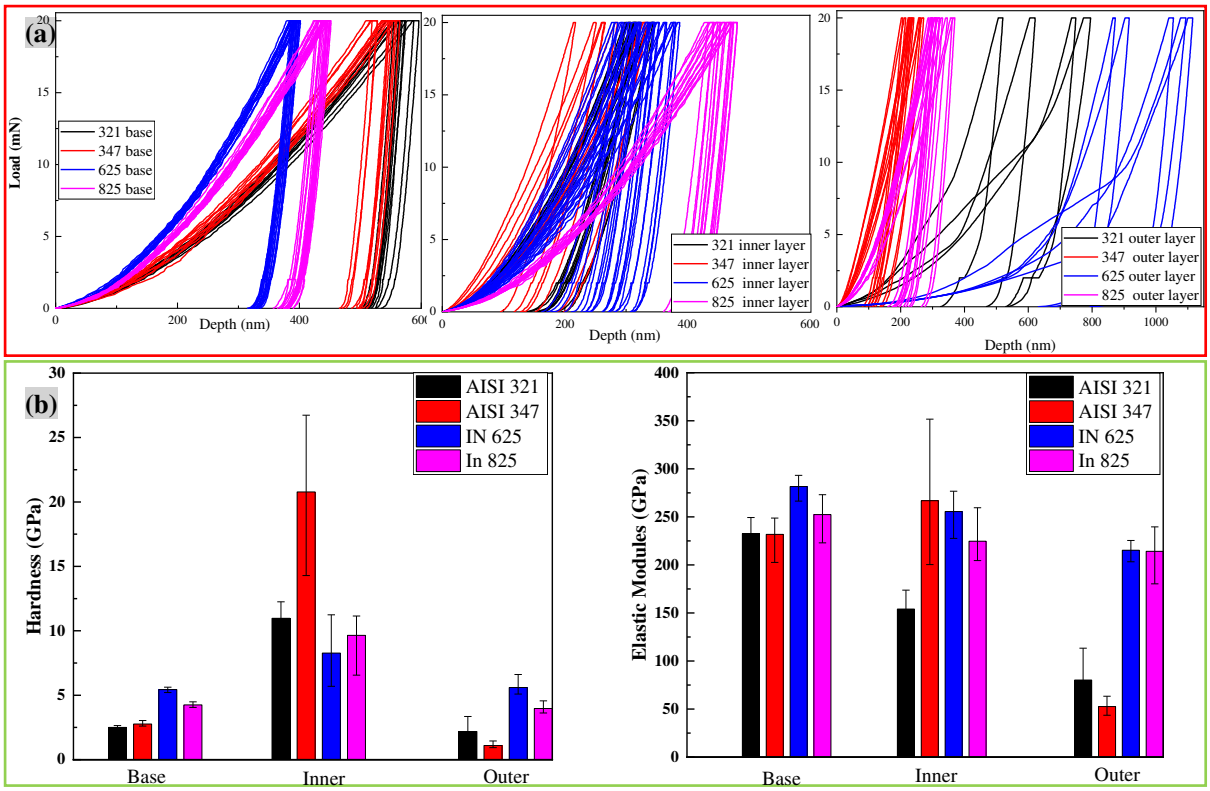

348

349 ***Figure 7: (a)Typical P-h curves of base material, inner layer and outer layer of AISI 321,***
350 ***AISI 347, IN 625 and In 825 and (b) corresponding harness and elastic modulus (samples***
351 ***after 600˚C isothermal in argon).***

352 ***Table 4 Linear coefficient of thermal expansion of metal and oxide [37] (temperature range***
353 ***100-800˚C)***

Metal/oxide	Thermal expansion coefficient (*10^{-6}) of Oxide [24]	Thermal expansion coefficient (*10^{-6}) of metal [24]	Poisson ratio
Fe-Fe_2O_3	12	15.3	0.25 [26]
Fe -Fe_3O_4	15		
Ni-NiO	17.1	17.6	
Cr-Cr_2O_3	7.3	9.5	0.33 [26]
Austenitic SS	-	16.0-19.5 (~17.4)	0.33
Inconel 625	-	13.1-17.8 (~17.8)	0.308

354
355
356
357
358

Table 5: Calculated thermal stress values (in GPa) between the various interfaces across the oxide – metal interface for the different combination of alloys, temperatures and test atmospheres investigated in this study.

Metal	YS/TS[#] At 600˚C	Argon at 600˚C		Air at 565˚C		Air at 600˚C	
		σ_1	σ'_1	σ_2	σ'_2	σ_3	σ'_3
AISI 321	0.13/0.38	-1.335	0.158	-0.348	*	-1.335	0.169
AISI 347	0.16/0.36	-2.31	0.138	-0.229	*	-2.31	0.087
IN 625	0.34/0.80	-2.20	0.491	-0.118	*	-0.125	*
In 825	0.15/0.48	-1.045	0.013	-0.969	*	-1.032	*

*: Not applicable with unavailable double layer.

[#] : YS and TS in the table stand for yield strength and tensile strength

4. Discussion

4.1 Effect of temperature on the corrosion characteristics and chemical evolution of interfacial oxide layers.

Figure 2 shows the weight loss and corrosion rate of stainless steels and Ni-based alloys after 7-day immersion test in solar salt as a function of temperature and gas atmospheres (air and Ar) respectively.

Referring to Figure 2 for all samples exposed to air, the corrosion rate increased with increasing test temperature from 565 to 600˚C. This trend shows good agreement with the literature [18]. This is likely due to the synergy of effect of temperature in terms of enhanced aggression of molten nitrate salts, and effect of temperature on changing the salt chemistry according to Equation 1 and Equation 2. It has been reported that increased corrosiveness of solar salt is likely from the decomposition of nitrate salt into nitrite salt and oxide ions when the salt's stability limit of 565˚C is surpassed [8, 38]. The equilibrium constant of Equation 1 and Equation 2 at 550˚C is reported to increase with increasing temperatures [38], thus accelerating the formation of oxide ions and expecting to enhance corrosivity of the salt.

From the XRD patterns and Raman spectra in Figure 3 and Figure 6 respectively, it is evident that the oxide layers formed on the surface of AISI 321 and AISI 347 in solar salt consists of different combination of iron oxide (Fe_2O_3), iron chromium spinel ($FeCr_2O_4$), sodium ferrite ($NaFeO_2$), and chromium oxide (Cr_2O_3). For IN 625, nickel oxides (NiO) were identified on the corrosion surface after test in air, and spinel of Ni and Fe was also observed on the Raman

spectra. NiO and mixed oxides of (Fe, Cr) are both identified on the samples of In 825 after test in air at 565 and 600˚C. $NaFeO_2$ was identified on the In 825 after test at 600˚C in air and under Ar atmosphere (see Figure 3 (d2)). This is strong indication that the specific combination of the interfacial oxide chemistries is directly dependent on the specific combination of test temperature and gas atmosphere. This will also determine the distribution of thermo-mechanical stress across the corrosion interface, as well as the overall corrosion characteristics of the molten salt – metal interface. The possible reactions pathway that guides the evolution of these interfacial corrosion oxides have been reported in previous studies [11, 29, 39].

For AISI 321, 347 and In 825 tested in air, $NaFeO_2$ was identified with a higher peak intensity at 600˚C (see Figure 3 (a2), (b2) and (d2)). It is known to be porous, non-protective [39], and with a high tendency to spall off as shown by region "S3" and "S6" in Figure 4 (a2) and (b2). After spallation of $NaFeO_2$, inner Cr-rich layer is then exposed to molten salt aggression as shown by region "S2" and "S7" in Figure 4 (a2) and (b2). This is a recipe for increased corrosion activities at the interface, especially as it has been reported that Cr-containing oxide was likely to be chemically dissolve into nitrate salt [40], therefore resulting in high corrosion rate in Figure 2. The spallation behaviours were also observed on and confirmed from the images from cross-sectional analysis in Figure 5 (a2) and (b2). It is also worth noting from Figure 5 that a double oxide layer was observed on the surfaces of stainless steels after test at 600˚C in air. This double oxide layer consists of an outer $Fe_2O_3/NaFeO_2$ and inner $FeCr_2O_4/Cr_2O_3$. The initially formed dense and protective Cr_2O_3/ $FeCr_2O_4$ layer prevents or retards the outward diffusion of alloys elements from the metal and inwards diffusion of oxide ions, while the outer Fe_2O_3 can provide some level of obstacle to the dissolution of Cr-rich later into molten salt. This synergy of barriers to continuous corrosion degradation mechanisms are destroyed with the formation and spallation of $NaFeO_2$ at temperatures higher than 600˚C [16], therefore resulting in higher corrosion rate and deeper corrosion depth.

Referring to SEM and cross-sectional images shown in Figure 4 and Figure 5 (a1) – (d1), relatively smooth surfaces were observed on the surfaces of all samples from test at 565°C in air to indicate the formation of a thin, dense and compact corrosion oxide layer on top of substrate metal. Polishing scratches are still visible on the surface of Ni-based alloy as evidence of supressed corrosion activities. Mild corrosion occurred on the samples at 565˚C in air. However, with the increase in temperature, the corrosion process is greatly accelerated, acting

in synergy with decomposed salt chemistries to drive new interfacial oxide formation and spallation.

4.2 Effect of test atmosphere on corrosion characteristics and chemical evolution of interfacial oxide layers.

As briefly mentioned earlier, the corrosion rate of studied alloys increases significantly with change in test atmosphere from air to argon at 600˚C. There is a general belief that oxidation and corrosion process should have been reduced in an inert protective atmosphere (argon for example). The reduced access to oxygen at salt-metal interfaces will likely reduce corrosion rate and localized attack due to inhomogeneity in the metal surface [16]. However, in this study, the obtained corrosion rate and the visible corrosion surface indicates that the corrosion process occurring under Ar atmosphere is more severe. This has been linked to a combination of specific reaction pathways that influences the corrosiveness of solar salt, the impact of delayed passivation from Cr_2O_3 due to slow availability of oxygen, and preferential formation of other non-protective oxide layers from previous publications [29, 41]. S. Bell [41] highlighted similar complexity related to corrosion in oxyanionic salt environment, and believed that basicity, and oxygen availability were responsible for the oxidation state of Fe and Cr, thus affecting the corrosion process.

Referring to the XRD patterns in Figure 3 (a2), (a3), and (b2), (b3) for stainless steel samples, Cr_2O_3 can be identified on the sample surface at 600˚C in air, but not in Ar atmosphere. It is expected that Cr_2O_3 forms as a passive oxide layer to protect the alloy element's outwards diffusion. The absence and/or delay in the formation of Cr_2O_3 on surface of samples under Ar atmospheres could be explained by unavailability and/or slower rate of diffusion of oxygen from air atmosphere. This has been observed in this study in the early stages of the evolution of the corrosion interface, and corroborates the observations of S. Bell [41]. Delayed passivation will also imply a non-equilibrium in favour of availability of Cr, Fe at the molten salt – alloy interface. The outward diffusion of these atoms from bulk material to the corrosion interface is driven by high temperature, resulting in high concentration of atoms at the interface. The absence of a prompt supply of oxygen to promote quick passivation of the interface will lead to the formation of thicker films of Cr-oxide layers as soon as oxygen becomes available via decomposition of nitrate to nitrite ions. Meanwhile, due to the high affinity of Fe and O, the formation and accumulation of Fe_2O_3 would promote the formation of $NaFeO_2$ by the Equation 6 (refer to supplementary file). This is shown by the higher peak intensity for $NaFeO_2$

in XRD patterns for test under Ar atmosphere than in air. Due to the porous and non-protective nature of $NaFeO_2$ (shown in Figure 4), thicker corrosion oxide scales are likely to form with a rather uneven thickness (as shown in Figure 5). The $NaFeO_2$ outer layer has a high tendency to spall off from the interface.

While the formation and spallation of $NaFeO_2$ is also observed in air, the initially formed inner Cr_2O_3 limits the outward diffusion of Fe and formation of Fe_2O_3, and therefore decrease the amount of $NaFeO_2$. Despite the observation of spallation in Figure 4 (a2) (b2), the corrosion oxide layer is thinner with a uniform thickness. The different source/pathways for the availability of oxygen to the corrosion interface in air and under Ar atmospheres directly affects the kinetics of Cr_2O_3 formation and the evolution of other interfacial oxide chemistries. A recent study confirmed [21] that the corrosion was accelerated when an inert argon environment was used in chloride/sulphate salt for nickel superalloy based on the basic salt corrosion mechanism and sodium metal oxides are favourable formed. In a previous study [29], it can be concluded that the salt aggressiveness increases with the increase of nitrite and oxide ions concentration by altering test atmosphere from air to Ar. Considering that the nitrite ions' oxidizing potential is much lower than that of the nitrate ions, the enhanced salt corrisivity is mainly caused by oxide ions from the complex decomposition of nitrate ions, as highlighted by work from Sötz [42, 43].

4.3 Correlation between interfacial stress distribution and the corrosion characteristics of interfacial oxides

In this study, the nano-mechanical properties of the interfacial corrosion oxide layers are investigated using nano-indentation technique in order to explain the relationship between spallation tendency of interfacial oxide layers and different stress levels across the metal – oxide interface. Referring to Figure 7, the hardness of base metal is higher than that of outer oxide layer but lower than that of inner oxide layer for Stainless steels. This indicates that the inner oxide layer is more dense, resilient and protective whilst outer oxide layer is porous, less adherent and resilient. As shown in Figure 5 (a3) (b3), the EDS line and mapping show that inner oxide layer is a Cr-rich layer and the porous outer Fe_2O_3/$NaFeO_2$ layer is characterised with a high-density of defects (e.g. pores and micro-cracks). The high hardness and stiffness associated with the continuous and compact inner oxide layer formed on the Stainless Steels samples (under Ar atmosphere at 600°C) indicates that the inner oxide layer is capable of providing an effective barrier to isolate the base metal from the oxidizing/corrosive molten salt

479 species. The high strength inner oxide layer also implies a higher resistance to cracking and/or
480 breakdown. For Ni-based alloys, the hardness difference between inner/outer oxide layers with
481 base metal is not as much as that of Stainless Steels. The hardness of base metal is almost same
482 with that of outer oxide layer and slightly lower than that of inner oxide layer. Referring to the
483 cross-sectional images shown in Figure 5, Cr-rich inner oxide layer was observed on the
484 surfaces of Ni-based alloys, while outer Fe-rich oxide layer was also observed to have more
485 pores and micro-cracks. In comparison with the outer oxide layers formed on all the studied
486 alloys, the hardness of outer oxide layer on Ni-based alloys are almost 2 times higher than that
487 on the stainless-steel samples, indicating the outer oxide layer is more resilient on Ni-based
488 alloys.
489 As briefly discussed earlier in this paper, stress associated with the formation and growth of
490 oxides on Stainless Steels and Ni-based alloys maintains protective under compressive stress.
491 Referring to the thermal stress calculated from the Equation 5 (listed in Table 5), the negative
492 sign of thermal stress between inner oxide layer and base metal also shows the manifestation
493 of compressive stress for all the alloys; with values ranging from 1.045 – 2.31 GPa for samples
494 tested under Ar atmosphere at 600˚C, 1.032 – 2.31 GPa for samples tested in air at 600˚C, to
495 0.118 - 0.348 GPa for samples test in air at 565˚C. This shows great agreement with the
496 observed higher strength of compact inner oxide layers and their relative resilience and
497 protectiveness. The tensile stress is imposed between inner oxide layer and outer oxide layers;
498 with values ranging from 0.013 – 0.491 GPa for samples tested under Ar atmosphere to 0.087
499 - 0.169 GPa for stainless steels samples tested in air at 600˚C. The tensile stress between inner
500 and outer oxide layers discussed above were calculated for corrosion interface with double
501 oxide layers; This was not applicable for the samples in air at 565˚C or the Ni-based alloys
502 samples at 600˚C in air (see Table 5).
503 These results clearly show that the compressive stress (negative sign) helps to keep the inner
504 oxide layer adhered to base metal and tensile stress (positive sign) leads to spallation of outer
505 oxide layer. The reasons responsible for the results above are probably attributed to the
506 structure of corrosion oxide layers, and the fact that inner oxide layer is initially formed as the
507 primary corrosion oxides with higher hardness and strength, and better adhered to the base
508 material. For stainless steel, the outer oxide layers (identified as $NaFeO_2$ by SEM) show lower
509 hardness than inner oxide layer. This is also confirmed from the stress calculation to be of poor
510 adherence to the inner Cr-rich oxide layer, and hence a recipe potential spallation to occur. The
511 tensile stress or thermally induced stress obtained between inner oxide and outer oxide layers
512 could also be partly attributed to the thermal expansion coefficient of inner Cr-based oxide

layer and outer Fe-based oxide layer. Therefore, the dense, more adherent and resilient inner oxide layer is less likely to spall off by thermo-mechanical stress effects after 7 days. However, this does not completely prevent the chemical attack of the inner oxide layer by aggressive molten salt species, particularly after the spallation of the outer oxide layers. As shown in Figure 5, the inner oxide layer was associated with less spallation after 7 days of immersion test in solar salt. It is believed from this study that the tendency for spallation of interfacial oxide layers to occur on the surface of these alloys is closely related to mechanical resilience of the interfacial oxide layers.

5. Conclusions

This study has successfully investigated the early stages (over 7 days) of corrosion behaviour of various alloys as a function of temperature and test atmosphere with the aim of correlating the overall corrosion characteristics at the molten salt – oxide – metal interface with the stress distribution across the interface. Here are the key conclusions.

1. High temperature and Ar test atmosphere acts in synergy to increase the corrosion rate up to ~3 fold for all alloys tested at 600°C This synergy is related to a combination of molten salt induced electrochemical activities, Arrhenius effect of high temperature on the rate of decomposition of nitrate salts to nitrite and delayed passivation by Cr_2O_3 due to lower availability of oxygen at the corrosion interface under Ar atmosphere.

2. The gas atmospheres and temperature synergistically controlled the overall corrosion characteristics at the molten salt – oxide – metal interface by its effect on the evolution of multiple interfacial corrosion oxide layers. Porous and less protective outer oxide layer consisting of a mixture of $NaFeO_2$ and Fe_2O_3 is kinetically favoured to form preferentially at 600°C under argon atmosphere.

3. The rate and sequence of evolution of interfacial oxide layers of varying chemistries directly correlate to the thermo-mechanical stress profile across the molten salt – oxide – metal interface. This also directly correlates with the tendency for spallation to occur and overall corrosion behaviour.

4. The spallation of sodium ferrite ($NaFeO_2$) formed on samples tested in air and under argon atmosphere at 600°C directly correlates to the tensile stress between the Cr-rich inner oxide layer and the $NaFeO_2$ layer.

5. The observed inner Cr-rich oxide layer is more adherent and resilient to degradation than the outer Na/Fe-based oxides. This was observed in this study to be due to the compressive stress between the inner Cr-rich oxide layer and the substrate material, and the destructive tensile stress between inner Cr-rich outer layer and outer Na/Fe-rich oxides layer to drive spallation process.

Dedicated to Late Prof. Anne Neville. OBE, FREng, FRS, FRSE, RAEng Chair in Emerging Technologies, University of Leeds.

Declaration of competing interest

The authors declared that they have no conflicts of interest to this conflict of interest to this manuscript.

Acknowledgements

The authors acknowledge the funding and support from Zhejiang JIULI Hi-tech Metals Co., Ltd.

Data Availability

Data will be made available on request.

CRediT authorship contribution statement

Qingyang Liu: Conceptualization, Methodology, Formal analysis, Investigation, Resources, Writing - original draft. **Chun Wang**: Supervision, Data collation, Methodology, Writing - review & editing. **Jiong Qian**: Review & editing. **Anne Neville**: Resources, Supervision. **Frederick Pessu**: Supervision, Writing - review & editing, Resources, Conceptualization.

References

[1] T.M. Meißner, C. Oskay, A. Bonk, B. Grégoire, A. Donchev, A. Solimani, M.C. Galetz, Improving the corrosion resistance of ferritic-martensitic steels at 600 °C in molten solar salt via diffusion coatings, Solar Energy Materials and Solar Cells, 227 (2021) 111105.

[2] W. Ding, T. Bauer, Progress in Research and Development of Molten Chloride Salt Technology for Next Generation Concentrated Solar Power Plants, Engineering, 7 (2021) 334-347.

[3] E. González-Roubaud, D. Pérez-Osorio, C. Prieto, Review of commercial thermal energy storage in concentrated solar power plants: Steam vs. molten salts, Renewable and Sustainable Energy Reviews, 80 (2017) 133-148.

[4] U. Pelay, L. Luo, Y. Fan, D. Stitou, M. Rood, Thermal energy storage systems for concentrated solar power plants, Renewable and Sustainable Energy Reviews, 79 (2017) 82-100.

[5] G. Alva, Y. Lin, G. Fang, An overview of thermal energy storage systems, Energy, 144 (2018) 341-378.

[6] K. Vignarooban, X. Xu, A. Arvay, K. Hsu, A.M. Kannan, Heat transfer fluids for concentrating solar power systems – A review, Applied Energy, 146 (2015) 383-396.

[7] M. Mehos, C. Turchi, J. Vidal, M. Wagner, Z. Ma, C. Ho, W. Kolb, C. Andraka, A. Kruizenga, Concentrating solar power Gen3 demonstration roadmap, in, National Renewable Energy Lab.(NREL), Golden, CO (United States), 2017.

[8] M. Walczak, F. Pineda, Á.G. Fernández, C. Mata-Torres, R.A. Escobar, Materials corrosion for thermal energy storage systems in concentrated solar power plants, Renewable and Sustainable Energy Reviews, 86 (2018) 22-44.

[9] A. Bonk, D. Rückle, S. Kaesche, M. Braun, T. Bauer, Impact of Solar Salt aging on corrosion of martensitic and austenitic steel for concentrating solar power plants, Solar Energy Materials and Solar Cells, 203 (2019).

[10] D. Nissen, D.J.I.C. Meeker, Nitrate/nitrite chemistry in sodium nitrate-potassium nitrate melts, 22 (1983) 716-721.

[11] Q. Liu, R. Barker, C. Wang, J. Qian, A. Neville, F. Pessu, The corrosion behaviour of stainless steels and Ni-based alloys in nitrate salts under thermal cycling conditions in concentrated solar power plants, Solar Energy, 232 (2022) 169-185.

[12] A. Bonk, S. Sau, N. Uranga, M. Hernaiz, T.J.P.i.E. Bauer, C. Science, Advanced heat transfer fluids for direct molten salt line-focusing CSP plants, 67 (2018) 69-87.

[13] R. Bradshaw, R.J.E.P.V. Carling, A review of the chemical and physical properties of molten alkali nitrate salts and their effect on materials used for solar central receivers, 1987 (1987) 959.

[14] M. Spiegel, J. Mentz, High temperature corrosion beneath nitrate melts, 65 (2014) 276-281.

[15] K.L. Summers, D.J.J.o.T.E.S. Chidambaram, Corrosion behavior of structural materials for potential use in nitrate salts based solar thermal power plants, 164 (2017) H5357.

[16] S. Bell, T. Steinberg, G. Will, Corrosion mechanisms in molten salt thermal energy storage for concentrating solar power, Renewable and Sustainable Energy Reviews, 114 (2019).

[17] G. Mohan, M.B. Venkataraman, J. Coventry, Sensible energy storage options for concentrating solar power plants operating above 600 °C, Renewable and Sustainable Energy Reviews, 107 (2019) 319-337.

[18] A.M. Kruizenga, D.D. Gill, M. LaFord, G.J.A.S.N.L.S.-. McConohy, Corrosion of High Temperature Alloys in Solar Salt at 400, 500, and 680 C, (2013).

[19] A. Bonk, M. Braun, V.A. Sötz, T. Bauer, Solar Salt – Pushing an old material for energy storage to a new limit, Applied Energy, 262 (2020) 114535.
[20] K. Vignarooban, X. Xu, K. Wang, E.E. Molina, P. Li, D. Gervasio, A.M. Kannan, Vapor pressure and corrosivity of ternary metal-chloride molten-salt based heat transfer fluids for use in concentrating solar power systems, Applied Energy, 159 (2015) 206-213.
[21] S. Bell, M.A. Rhamdhani, T. Steinberg, G. Will, Aggressive corrosion of C-276 nickel superalloy in chloride/sulphate eutectic salt, Solar Energy, 227 (2021) 557-567.
[22] R.W. Bradshaw, S.H. Goods, Corrosion resistance of stainless steels during thermal cycling in alkali nitrate molten salts, in, Sandia National Laboratories, 2001.
[23] A. Soleimani Dorcheh, R.N. Durham, M.C. Galetz, Corrosion behavior of stainless and low-chromium steels and IN625 in molten nitrate salts at 600 °C, Solar Energy Materials and Solar Cells, 144 (2016) 109-116.
[24] Y. Yin, Q. Tan, Y. Zhao, Q. Sun, Z. Shi, M. Bermingham, W. Zhuang, H. Huang, M.-X. Zhang, A cost-effective Fe-rich compositionally complicated alloy with superior high-temperature oxidation resistance, Corrosion Science, 180 (2021) 109190.
[25] Q. Tan, N. Mo, C.-L. Lin, Y. Zhao, Y. Yin, B. Jiang, F. Pan, A. Atrens, H. Huang, M.-X. Zhang, Generalisation of the oxide reinforcement model for the high oxidation resistance of some Mg alloys micro-alloyed with Be, Corrosion Science, 147 (2019) 357-371.
[26] P. Ramos, R.S. Coelho, F. Soldera, H.C. Pinto, F. Mücklich, P. Brito, Residual stress analysis in thermally grown oxide scales developed on Nb-alloyed refractory austenitic stainless steels, Corrosion Science, 178 (2021) 109066.
[27] E. Pu, W. Zheng, J. Xiang, Z. Song, J. Li, Hot deformation characteristic and processing map of superaustenitic stainless steel S32654, Materials Science and Engineering: A, 598 (2014) 174-182.
[28] N. Birks, G.H. Meier, F.S. Pettit, Introduction to the high temperature oxidation of metals, Cambridge university press, 2006.
[29] Q. Liu, J. Qian, R. Barker, C. Wang, A. Neville, F. Pessu, Effect of thermal cycling on the corrosion behaviour of stainless steels and Ni-based alloys in molten salts under air and argon, Solar Energy, 238 (2022) 248-257.
[30] G.M. Pharr, W.C. Oliver, Measurement of Thin Film Mechanical Properties Using Nanoindentation, MRS Bulletin, 17 (1992) 28-33.
[31] G. McConohy, A. Kruizenga, Molten nitrate salts at 600 and 680°C: Thermophysical property changes and corrosion of high-temperature nickel alloys, Solar Energy, 103 (2014) 242-252.
[32] G. Pharr, W.J.M.B. Oliver, Measurement of thin film mechanical properties using nanoindentation, 17 (1992) 28-33.
[33] F. Rahmawati, A.A. Kusumaningtyas, T.E. Saraswati, A. Prasetyo, V. Suendo, Mn-doped NaFeO2 from a low purity-Fe precursor and its performance as cathode for Sodium-Ion Battery, Inorganic and Nano-Metal Chemistry, 51 (2021) 383-390.
[34] K.F. McCarty, D.R. Boehme, A Raman study of the systems Fe3−xCrxO4 and Fe2−xCrxO3, Journal of Solid State Chemistry, 79 (1989) 19-27.
[35] P. Colomban, S. Cherifi, G. Despert, Raman identification of corrosion products on automotive galvanized steel sheets, 39 (2008) 881-886.
[36] D.L.A. de Faria, S. Venâncio Silva, M.T. de Oliveira, Raman microspectroscopy of some iron oxides and oxyhydroxides, 28 (1997) 873-878.
[37] P. Hancock, R. Hurst, The mechanical properties and breakdown of surface oxide films at elevated temperatures, in: Advances in corrosion science and technology, Springer, 1974, pp. 1-84.

[38] Á.G. Fernández, L.F. Cabeza, Molten salt corrosion mechanisms of nitrate based thermal energy storage materials for concentrated solar power plants: A review, Solar Energy Materials and Solar Cells, 194 (2019) 160-165.
[39] Q. Liu, J. Qian, A. Neville, F. Pessu, Solar thermal irradiation cycles and their influence on the corrosion behaviour of stainless steels with molten salt used in concentrated solar power plants, Solar Energy Materials and Solar Cells, 251 (2023) 112141.
[40] O. Ahmed, Corrosion behaviour of AISI 304 stainless steel in contact with eutectic salt for concentrated solar power plant applications, (2013).
[41] S. Bell, M.W.M. Jones, E. Graham, D.J. Peterson, G.A. van Riessen, G. Hinsley, T. Steinberg, G. Will, Corrosion mechanism of SS316L exposed to NaCl/Na2CO3 molten salt in air and argon environments, Corrosion Science, 195 (2022) 109966.
[42] V.A. Sötz, A. Bonk, J. Steinbrecher, T. Bauer, Defined purge gas composition stabilizes molten nitrate salt - Experimental prove and thermodynamic calculations, Solar Energy, 211 (2020) 453-462.
[43] J. Steinbrecher, A. Bonk, V.A. Sötz, T. Bauer, Investigation of Regeneration Mechanisms of Aged Solar Salt, 14 (2021) 5664.